RESEARCH ARTICLE

Editor's Choice

ADVANCED MATERIALS INTERFACES Open Access

www.advmatinterfaces.de

Tunable LiZn-Intermetallic Coating Thickness on Lithium Metal and Its Effect on Morphology and Performance in Lithium Metal Batteries

*Marlena M. Bela, Christina Schmidt, Kerstin Neuhaus, Tobias Hering, Marian C. Stan, Martin Winter, and Markus Börner**

Lithium metal batteries are promising next-generation rechargeable batteries with high energy density. However, the high reactivity of lithium metal leads to an undesirable growth of high surface area lithium during electrodeposition and -dissolution and remains a key challenge that must be addressed to enable commercialization. Modification of the Li metal surface to obtain protective coatings is a common method to overcome these challenges. In this study, the influence of the thickness of an intermetallic coating on Li metal is investigated after application by means of thermal evaporation. In addition, the relevance of pre-treatments in reducing the native layer thickness and surface roughness by roll-pressing Li metal prior to coating is demonstrated. Morphological analyses are performed on cross-sections prepared under cryogenic conditions to investigate the origin of high surface area lithium growth and coating cracks after electrodeposition and -dissolution processes. The results obtained support the conclusion that the exclusive combination of roll-pressed Li metal foil followed by coating reduces overvoltage and improves cycle life at elevated current densities.

1. Introduction

The incorporation of renewable energy sources, such as wind and solar energy is essential to promoting sustainability in the energy sector. However, their intermittent energy supply presents practical challenges that need to be addressed.[1,2] Suitable energy storage systems, such as batteries, are needed to cache the generated electric power and can additionally realize an emission-free automotive sector via electric vehicles (EVs) or as stationary energy battery storage systems for private households and industry.[3,4] To date, lithium-ion batteries (LIBs) dominate the global market of rechargeable batteries for portable electronic devices and were already been successfully implemented in EVs, while the demand for higher specific energy [Wh kg^{-1}] and energy densities [Wh L^{-1}] continues to increase.[5–7] In the search for alternative battery systems and to meet these demands, lithium metal (Li metal) as a negative electrode (anode) has regained increasing interest due to its high theoretical capacity (3860 mAh g^{-1}) and low electrode potential, i.e., −3.04 V versus standard hydrogen electrode.[1,8] Due to its high reactivity, lithium forms a protective layer known as solid electrolyte interphase (SEI) immediately after contact with the electrolyte, which is composed of organic and inorganic electrolyte decomposition products.[9–12]

The mosaic structure of the SEI promotes a preferential electrodeposition/-dissolution in areas of higher Li ion conductivity, resulting in the formation of high surface area lithium (HSAL), with a mossy, dendritic, or granular morphology.[13–15] The associated volume changes during Li electrodeposition/-dissolution and the resulting dynamic anode surface cause the SEI to crack and expose fresh lithium, which reacts with the electrolyte again, resulting in further electrolyte consumption, SEI repair, and HSAL growth. These mechanisms pose serious safety risks due to electrolyte depletion, inactive or dendritic HSAL that can penetrate the separator and cause short circuits, and the high reactivity of HSAL in the presence of electrolytes causing reduced overall thermal stability.[8,14,16–18] To enable the commercialization of Li metal-based batteries, strategies have been developed to suppress these undesired reactions, e.g., the addition of additives in the liquid electrolyte,[19] development of suitable 3D hosts,[20–22] surface micropatterning to increase the surface area,[14,23] and implementation of a protective coating, such as an artificial SEI by in situ and ex situ Li metal surface modification.[24–27] The approach to modify the

M. M. Bela, T. Hering, M. Winter, M. Börner
MEET Battery Research Center
University of Münster
Corrensstraße 46, 48149 Münster, Germany
E-mail: markus.boerner@uni-muenster.de

C. Schmidt, K. Neuhaus, M. C. Stan, M. Winter
Helmholtz Institute Münster (HI MS)
IEK-12
Forschungszentrum Jülich GmbH
Corrensstraße 46, 48149 Münster, Germany

The ORCID identification number(s) for the author(s) of this article can be found under https://doi.org/10.1002/admi.202300836

DOI: 10.1002/admi.202300836

surface of Li anodes to create desired interphase properties was frequently adopted to improve the lifetime of lithium metal batteries (LMBs).[28] Artificial protective coatings based on organic, inorganic, or intermetallic materials were intensively studied with the purpose of determining the impact of the different characteristics of each coating.[29] Li-containing intermetallic protective coatings Li*M* (*M* = Au, Ag, In, Bi, Sn, Zn, Sn, etc.) have gained increasing interest because they can reduce detrimental side reactions due to the higher chemical potential than pure Li metal and produce a more uniform Li deposition/-dissolution, based on the increased Li-ion diffusion coefficient of the Li*M*-coating compared to bare Li metal.[30,31] There are several methods of depositing an intermetallic protective coating, such as mechanical processes,[32] wet-chemical,[33,34] and gas phase processes.[35–37] All of these methods share the common characteristic of using the reactivity of lithium to produce a mixed intermetallic composite or alloy at the interface.[31]

Sputter deposition was often employed as a physical vapor deposition (PVD) technique for Li metal coatings due to the solvent- and organic additive-free fabrication of thin coatings with a tunable thickness. The replaceable sputter target enables a fast screening of various intermetallic phases, as shown in recent studies.[35,38–41] However, sputter deposition suffers from low efficiency due to low deposition rates ($<10^{-4}$ g cm^{-2} s^{-1}) and high energy consumption during the sputtering process that could hinder the industrial application. An alternative PVD technique with a better cost and energy efficiency is the thermal evaporation of metals, which was not employed as a coating technique on Li metal foils, yet.[38,42] The high-purity source materials are inexpensive compared to sputter targets affecting directly the quality and purity of the coating. In addition, the higher deposition rate (10^{-3} g cm^{-2} s^{-1}) enables a reasonable throughput application among the PVD techniques and deposited coatings with good purity and adhesion.[42,43]

In the process of finding a suitable metal for an intermetallic protective coating on Li metal, three factors must be considered: 1) Low cost of the source material 2) non-toxicity, and 3) a high Li diffusion coefficient. This leads to the exclusion of Au, Ag, In, or Sb due to high cost or toxicity, leaving materials such as Sn and Zn as promising candidates. Zn-coatings on Li metal via sputter deposition were thoroughly investigated in recent studies due to their fast intermetallic phase formation, high Li ion diffusion coefficient and chemical stability against electrolytes.[35,39–41,44–46] However, it is important to optimize the coating thickness of the intermetallic coating on Li metal and to study the influence of the subjacent native layer on the formation of the intermetallic coating, regarding homogeneity of the coating and the electrochemical performance.

In this study, thermal evaporation was employed as an energy- and cost-efficient PVD technique to form a Zn-coating on Li metal. The influence of the intermetallic coating thickness on electrodeposition/-dissolution processes as well as the long-term cyclability was investigated. The first part focuses on the deposition of different coating thicknesses of Zn on untreated Li foil with a native layer. The second part illustrates the effect of roll-pressing Li metal foil, which results in thinning of the native layer and reduction of surface roughness prior to the Zn coating.

2. Results and Discussion

2.1. Thickness Effect of Intermetallic Coating on Pristine Li Metal Foil

Li metal shows high reactivity toward liquid electrolytes due to its low standard reduction potential. One option to reduce reactivity is the application of coatings to protect the subjacent lithium from decomposition reaction with the electrolyte and an increase of the Li-ion flux. In this regard, an intermetallic coating was deposited on lithium by PVD via thermal evaporation of Zn. Zn was the material of choice due to its low cost and the high Li ion diffusion coefficient of the LiZn-intermetallic coating.[46] Thermal evaporation (Figure S1, Supporting Information) was employed as a coating method as a cost and energy-efficient PVD technique on Li metal that creates a dense, homogeneous coating with tunable thickness. In order to examine the influence of the intermetallic coating thickness on Li metal during electrodeposition/-dissolution processes, 100, 250, and 500 nm Zn were deposited on untreated Li foil (130 µm, $Li_{pristine}$).

The Li surface showed a uniform golden color after Zn-coating, indicating the formation of the LiZn-intermetallic phase over the entire Li metal surface as depicted in the optical images in Figure S2 (Supporting Information).[35,39,40] Elemental mapping exhibited a homogeneous distribution of Zn at the surface (Figure S3, Supporting Information). X-ray diffraction (XRD) patterns (Figure S4, Supporting Information) showed reflections at 24.8°, 41.1°, 48.5°, 59.4°, 65.3°, and 74.7° that match with the LiZn-intermetallic phase (PDF-03-065-3016) and the reflections at 36.3°, 52.2°, and 65.1° match with Li metal (PDF 01-071-4605). Overall, the XRD analysis exhibited a mixed phase consisting of a Li- and LiZn-phase as predicted for LiZn alloys with an intensity increase of the intermetallic phase reflection with a thicker coating.[47,48]

Figure 1 displays the surface and cross-sections prepared under cryogenic conditions of $Li_{pristine}$ and coated $Li_{pristine}$ with 100, 250, and 500 nm Zn (further referred to as $LiZn_{100}$, $LiZn_{250}$, and $LiZn_{500}$). The coating thickness of the intermetallic LiZn-phase was determined with cross-sectional analysis (Figure 1). Scanning electron microscopy (SEM) top-view images showed linear patterns on the $Li_{pristine}$ surface, which are presumably formed during extrusion as a part of the Li foil production process (Figure 1a). These patterns remained evident in the Zn-coated Li foils (Figure 1b–d), indicating that the surface structure of $Li_{pristine}$ affects the coating morphology.[14,49]

Figure 1b–d,f–h and Figure S3 (Supporting Information) showed a homogeneous coating with a uniform distribution of Zn at the Li surface. The volume of the coating expanded during the formation of the intermetallic phase, as depicted in the cross-section images prepared under cryogenic conditions to avoid morphological changes of lithium or the Li-containing intermetallic coating (Figure 1f–h). During the formation of the intermetallic coating, Li atoms were embedded into the deposited zinc hcp crystal structure (hexagonal closest packed, A3) to form the intermetallic NaTl-type (B3) crystal structure, which caused a volumetric expansion.[48] For $LiZn_{100}$ an increase in thickness of the intermetallic phase to 100–110 nm was observed, $LiZn_{250}$ showed a thickness of 600–800 nm and $LiZn_{500}$ 1.2–1.4 µm, resulting in a pronounced volume expansion for $LiZn_{250}$ and

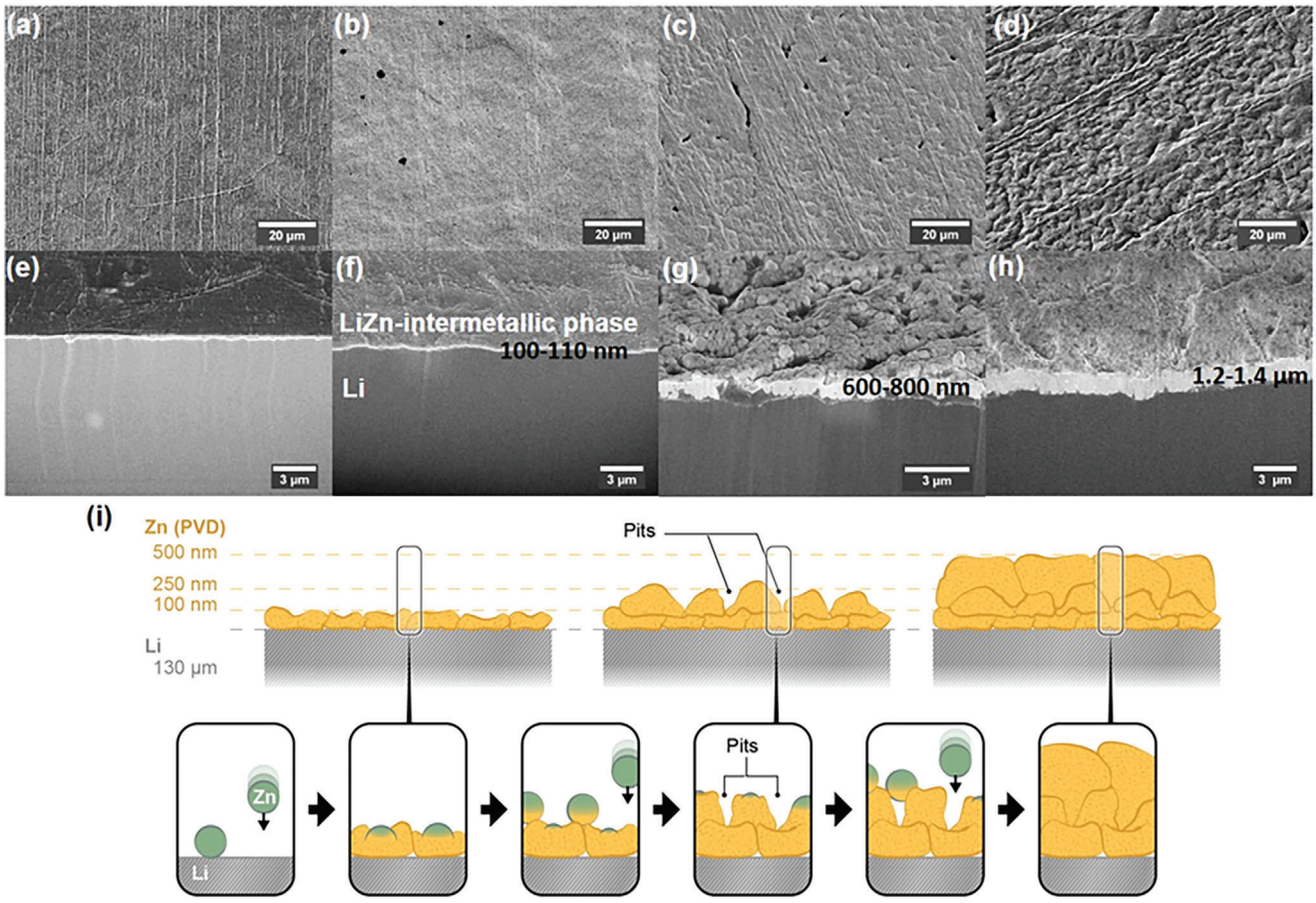

Figure 1. SEM investigations of the surface morphology of a) $Li_{pristine}$, b) $LiZn_{100}$, c) $LiZn_{250}$, and d) $LiZn_{500}$ and the corresponding cryo-FIB cross-sections of e) $Li_{pristine}$, f) $LiZn_{100}$, g) $LiZn_{250}$, and h) $LiZn_{500}$. Graphic illustration of the coating morphology shown for i) $LiZn_{100}$, j) $LiZn_{250}$, and k) $LiZn_{500}$.

$LiZn_{500}$. The formation of the intermetallic phase caused an increase in surface roughness with thicker coating, which was detected in the laser scanning microscopy (LSM) images (Figure S5, Supporting Information) and confirmed by the corresponding roughness parameter determination (**Figure 2a**; Table S2, Supporting Information). Another reason for the high roughness was based on the growth mechanism of the deposited zinc coating, described by the island growth model (Volmer–Weber model). In the initial stage, gaseous Zn atoms were deposited on the Li surface and condensed rather finely dispersed. Subsequently, the intermetallic phase was formed, and due to the volume expansion, deposited LiZn phases coalesced as schematically illustrated in Figure 1i. For $LiZn_{250}$ a higher amount of Zn was deposited and a stronger Zn—Zn interaction than Zn—Li interaction caused island growth which was still evident after the formation of the intermetallic phase resulting in a higher surface roughness and apparent voids within the coating (Figure 1i). After deposition of another 250 nm Zn, these islands intergrow with each other ($LiZn_{500}$) and form a continuous coating with a corrugated morphology due to the volume expansion after the intermetallic phase formation (Figures 1i and 2c).[50] Overall, a homogeneous LiZn-intermetallic coating with adjustable thickness was deposited on Li metal with the thermal evaporation technique, as shown by the optical images and XRD results. SEM and LSM analysis revealed an increased surface roughness due to the island growth mechanism during Zn-deposition and the LiZn-intermetallic phase formation. Based on the Kelvin probe force microscopy (KPFM) measurements, the surface potential φ_{SP} and roughness parameter SA of $Li_{pristine}$ and coated $Li_{pristine}$ surfaces were determined (Figure 2b–d; Figure S7, Table S2, Supporting Information), while the detailed theoretical background is described in the Supporting Information.

The roughness parameter obtained by KPFM revealed a similar trend to the LSM roughness parameter. Surface potential measurements of $Li_{pristine}$ showed a negative value (φ_{SP} = −350 to −400 mV), whereas the surface potential of pure lithium should be in the range of +1.4 V (Figure 2b; Figure S6, Supporting Information). The negative value was caused by an inorganic and insulating native layer based on Li_2CO_3, LiOH, and Li_2O components, formed due to the reactivity of lithium in the atmosphere and was slightly increasing during storage in the glovebox.[51–53] Roll-pressing Li metal foil can dilute and homogenize the native layer improving lithium electrodeposition/-dissolution, as Becking et al. demonstrated.[49] Herein, roll-pressed Li electrodes (Li_{rp}) showed less surface roughness and a positive surface potential (φ_{SP} = +875 to +1000 mV), with a value closer to the expected

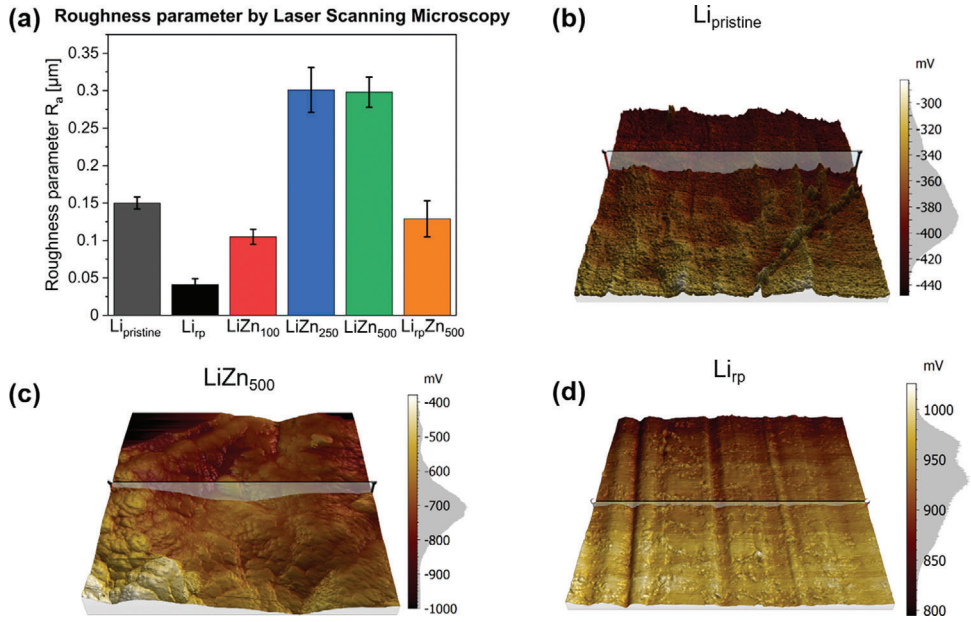

Figure 2. a) Roughness parameter R_a of $Li_{pristine}$, Li_{rp}, $LiZn_{100\text{-}500}$, and $Li_{rp}Zn_{500}$ determined by LSM. KPFM images with a 10 × 10 µm2 frame of b) $Li_{pristine}$, c) $LiZn_{500}$, and d) Li_{rp} with a color bar of the determined surface potential in each region.

range for pure Li metal (Figure 2d; Table S2, Supporting Information) resulting in a successful dilution of the native film.

Subsequently, the different intermetallic coating thicknesses on lithium were electrochemically characterized in a symmetric cell with $Li_{pristine}||Li_{pristine}$ and $LiZn_{100\text{-}500}||LiZn_{100\text{-}500}$. **Figure 3a** shows the galvanostatic nucleation overvoltage during Li electrodeposition within the first cycle. The nucleation overvoltage is defined as the difference between the sharp tip voltage and the flat voltage platform as depicted for $LiZn_{500}$ in Figure 3a.[54] A steady increase in nucleation overvoltage with increasing coating thickness ($Li_{pristine}$: −0.25 V; $LiZn_{100}$: −0.30 V, $LiZn_{250}$: −0.38 V, $LiZn_{500}$: −0.49 V; Table S1, Supporting Information) indicated a higher kinetical hindrance with respect to Li-ion mobility and electrodeposition for a thicker intermetallic coating on $Li_{pristine}$. These results appeared counterintuitive since a decrease in overvoltage was reported for Li alloy-forming metals, such as Au, Ag,

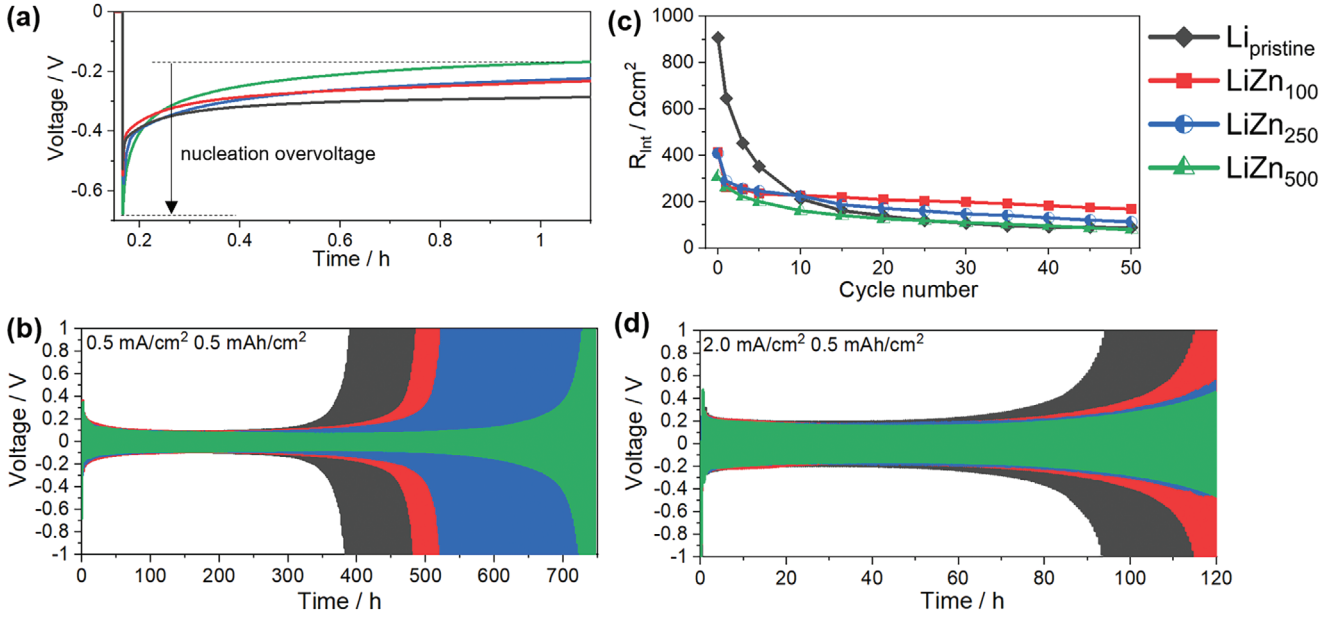

Figure 3. Comparison of a) overvoltage profiles from the first electrodeposition, b) evolution of R_{int} during the first 50 cycles and galvanostatic cycling at 0.5 mA cm^{-2} and EIS measured in a frequency range between 0.1 MHz and 0.1 Hz. c) 0.5 mA cm^{-2} and d) 2.0 mA cm^{-2} with a capacity of 0.5 mAh cm^{-2} of symmetric cells with $Li_{pristine}$ (black), $LiZn_{100}$ (red), $LiZn_{250}$ (blue), and $LiZn_{500}$ (green).

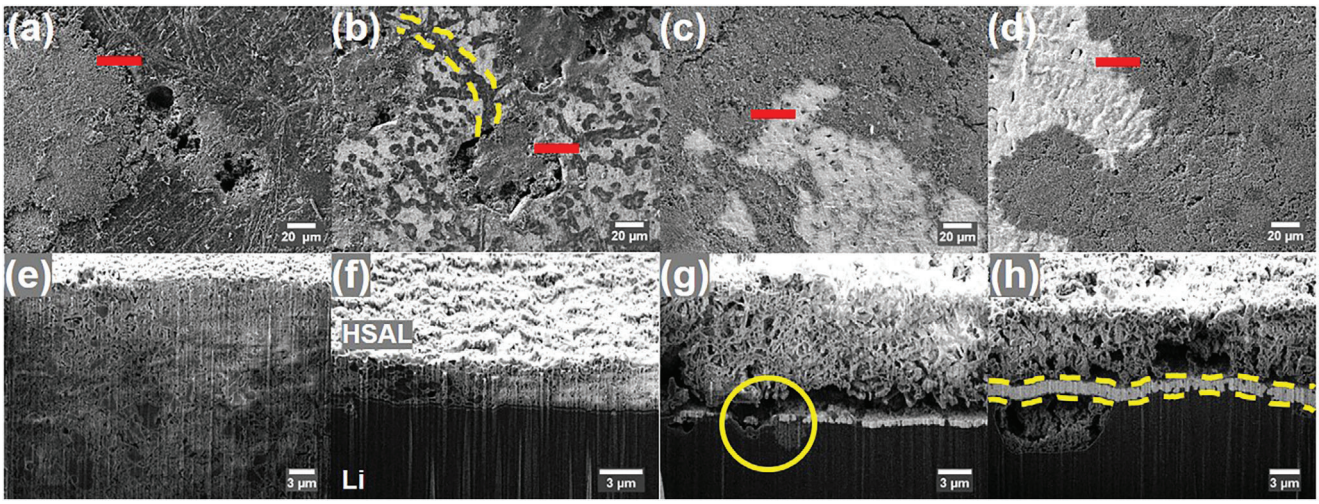

Figure 4. SEM investigations of the surface morphology of a) $Li_{pristine}$, b) $LiZn_{100}$, c) $LiZn_{250}$, and d) $LiZn_{500}$ and the corresponding cryo-FIB cross-sections of e) $Li_{pristine}$, f) $LiZn_{100}$, g) $LiZn_{250}$, and h) $LiZn_{500}$ after 20 cycles with 0.5 mA cm^{-2} and 0.5 mAh cm^{-2}. The dark area represents Li metal and the light area is HSAL, as demonstrated in (f).

and Zn. [55] The observed phenomenon was attributed to the subjacent native layer of $Li_{pristine}$ in combination with the intermetallic coating. The inorganic and insulating components provided an additional barrier to Li ions during electrodeposition, resulting in a higher nucleation overvoltage and can consequently influence cycling performance.[49,52,56] Figure 3a illustrates that the absence of Li metal roll-pressing prior to coating resulted in an increase of the nucleation overvoltage. The anticipated nucleation overvoltage drop was evident in the long-term cycling test at low current densities for $LiZn_{500}$ after 300–500 cycles (Figure 3c). The overvoltage drop might originate from the HSAL growth on top of the intermetallic coating due to a surface area increase (**Figure** 4d,h), or from the native layer dilution during electrodeposition/-dissolution into the Li bulk.

The effective protection of the intermetallic coating against electrolyte decomposition at the Li surface was confirmed by the corresponding impedance data shown in Figure 3b and interpreted as demonstrated in Figure S8 (Supporting Information). $Li_{pristine}$ has the highest interphase resistance R_{int} before electrodeposition/-dissolution (0 cycles), due to an instant formation of a resistive SEI based on the Li surface reaction with the electrolyte. In contrast, the thickest Zn-coating ($LiZn_{500}$) revealed the lowest R_{int} since the formed LiZn-intermetallic coating prevents electrolyte decomposition. $LiZn_{100}$ and $LiZn_{250}$ showed an enhanced R_{int} compared to $LiZn_{500}$. This indicated that $LiZn_{100}$ offers less effective protection against electrolyte decomposition due to its thin intermetallic coating, while $LiZn_{250}$ showed reduced effectiveness due to the presence of voids within the coating (Figure 1c,g) that compromise its protective capabilities. The higher R_{int} values of $LiZn_{100}$ and $LiZn_{250}$ compared to $LiZn_{500}$ are also observed with progressing cycle numbers and confirmed less effective protection of the Li surface during electrodeposition/-dissolution. After the first 10 cycles, the R_{int} of $Li_{pristine}$ decreased considerably from 1606 to 376 Ω implying a surface area increase.[57] R_{int} of $LiZn_{500}$ remained the lowest with increasing cycle number indicating a good Li ion conductivity through the intermetallic coating, enhanced Li electrodeposition/-dissolution and constant protection against electrolyte decomposition.

The influence of the different Zn-coatings was most apparent at low current densities (Figure 3c for 0.5 mA cm^{-2}), resulting in a ≈90% increase in cycle number from $Li_{pristine}$ to $LiZn_{500}$ before reaching the cut-off voltage ($Li_{pristine}$: 390 cycles, $LiZn_{500}$: 735 cycles). At higher current densities, the increase in cycle number before reaching the cut-off voltage was ≈25% for $LiZn_{500}$ compared to $Li_{pristine}$, with a less pronounced effect than observed at lower current densities (Figure 3d for 2.0 mA cm^{-2}; Figure S9a (Supporting Information) for 1.0 mA cm^{-2}). Overall, better protection against electrolyte decomposition was observed with a thicker intermetallic coating. During prolonged electrodeposition/-dissolution, the SEI of $Li_{pristine}$ or thinner intermetallic coatings such as $LiZn_{100}$ and $LiZn_{250}$ cracked and exposed fresh lithium that will react with the electrolyte.

A thicker intermetallic coating, such as $LiZn_{500}$, allowed the subjacent Li reservoir to remain protected longer during electrodeposition/-dissolution, as cracks in the coating and dissolution within the Li bulk emerged later. This mechanism was observed in the cross-sections prepared under cryogenic conditions that were performed in areas with visible HSAL next to a pristine surface without cracks, as depicted in Figure 4a–d with the red bar. For post-mortem analysis the symmetric cells were disassembled and analyzed after 20 cycles (0.5 mA cm^{-2}, Figure 4). For $Li_{pristine}$ (Figure 4a,e), the characteristic pit formation and irregular HSAL growth upon electrodeposition/-dissolution was observed.[35] $LiZn_{100}$ (Figure 4b,f) revealed an increased pit formation in regions with a cracked intermetallic coating. These "weak spots" were located at the natural grain boundaries of Li metal (Figure 4b, between the dashed line) on which the intermetallic coating was oriented. The heterogeneous chemical composition of the native layer showed surface grain boundaries with a lower surface resistance and higher Li ion diffusion coefficient. Li ions deposit preferentially in the vicinity of surface grain boundaries, as Sanchez et al. demonstrated in an *operando* microscopy study.[58] Consequently, a preferred Li

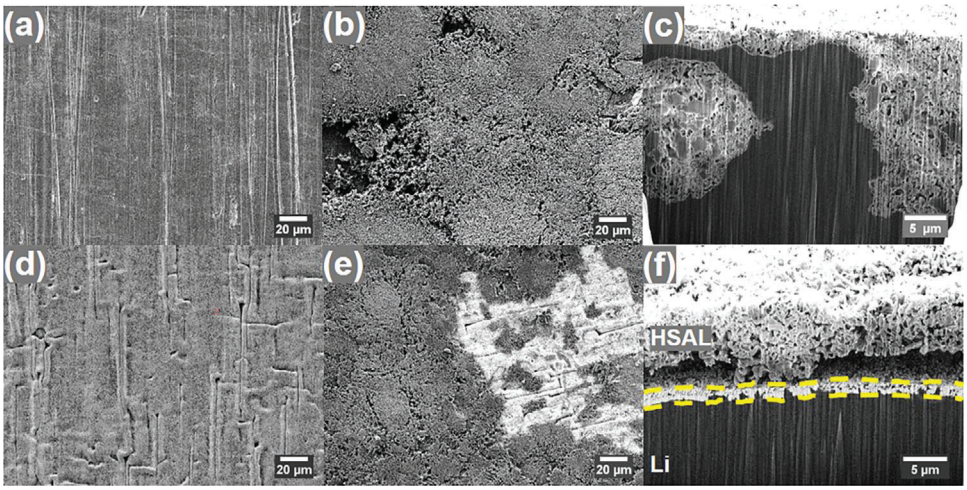

Figure 5. Top-view SEM images and cryo-FIB cross-sections of a–c) Li_{rp} and d–f) $Li_{rp}Zn_{500}$. a,d) Top-view images before cycling and b,c,e,f) after 20 cycles with 0.5 mA cm^{-2} and 0.5 mAh cm^{-2} for Li_{rp} and $Li_{rp}Zn_{500}$.

electrodeposition/-dissolution was observed alongside the subjacent grain boundaries of the $Li_{pristine}$ foil. The cross-section images (Figure 4f) revealed the absence of an intermetallic coating in regions of HSAL growth, due to the complete cracking of the coating and dissolution within the HSAL and Li bulk. The top-view image of cycled $LiZn_{250}$ displayed a more uniform HSAL growth on the surface and an intact coating in areas without HSAL growth. Cracking, dissolution of the intermetallic coating, pit formation, and deposited lithium under the coating were evident in the cross-section images (Figure 4c,g, circled area). The electrodes of the cycled $LiZn_{500}$||$LiZn_{500}$ cells exhibited dense HSAL deposits on the surface and an intact intermetallic coating in regions without HSAL growth (Figure 4d). The cross-section image from regions with HSAL growth on the electrode surface revealed an intact intermetallic coating with a curvature (Figure 4h, between the dashed line). Apart from the HSAL growth on the intermetallic surface, Li deposits were observed underneath the coating, especially in areas with higher curvature.

In summary, electrochemical and morphological analyses revealed that $LiZn_{500}$, based on a 500 nm Zn-coating on lithium has the most positive effect with respect to the protection of the Li anode and enables a prolonged cycle life. However, the intermetallic coating showed that the Li surface roughness caused higher curvature, which is predestined to crack formation during cycling and accelerated HSAL growth. Consequently, a smoother surface with a thinner native layer should improve the coating properties and thus the electrochemical performance and cycling stability. Therefore, the optimization of the intermetallic coating by roll-pressing $Li_{pristine}$ foil before Zn deposition was studied.

2.2. Influence of Roll-Pressing and Coating on the Li Metal

The initial topology of the Li metal anode was shown to affect the quality of the deposited Zn-coating (Figure 1), due to the passed-on inhomogeneity and curvature to the applied LiZn-intermetallic coating. It was recently demonstrated that roll-pressing of Li foil can improve the electrochemical performance and topological characteristics through a dilution and homogenization of the native layer accompanied by reduced surface roughness.[49,59] Therefore, roll-pressing Li foil was combined with a LiZn-intermetallic coating to study the effect on the obtained surface and its electrodeposition/-dissolution behavior. For this purpose, Li foil was roll-pressed from 500 to 130 µm, and Li_{rp} was coated with 500 nm Zn (further referred to as $Li_{rp}Zn_{500}$), as the coating thickness was most promising to enhance the cycle lifetime.

Subsequently, the roughness parameter and surface potential φ_{SP} determined by KPFM and LSM of $Li_{pristine}$, Li_{rp}, $LiZn_{500}$, and $Li_{rp}Zn_{500}$ foils were compared. Figure 2d and Tables S2 and S3 (Supporting Information) indicate that roll pressing of $Li_{pristine}$ produces the desired reduction of the surface roughness for Li_{rp} and $Li_{rp}Zn_{500}$. **Figure 5**a,d displays the top-view images of Li_{rp}, and $Li_{rp}Zn_{500}$ before galvanostatic cycling and demonstrated a smoother surface due to roll-pressing before Zn-coating compared to the pristine surfaces of $Li_{pristine}$ and $LiZn_{500}$ (Figure 1a,d). Particularly, $Li_{rp}Zn_{500}$ showed a more homogeneous structure with less curvature after forming the intermetallic phase, in contrast to $LiZn_{500}$ (Figure 1d).

KPFM images in Figure 2b–d and Figure S7 (Supporting Information) illustrate the determination of the surface potential and roughness of Li_{rp} and $Li_{rp}Zn_{500}$. The surface potential for $LiZn_{500}$ was found to range from $\varphi_{SP} = -575$ to -730 mV and for $Li_{rp}Zn_{500}$ from $\varphi_{SP} = -550$ to -750 mV, whereby pure zinc showed a surface potential of $\varphi_{SP} = -660$ to -845 mV. The negative surface potential close to pure zinc implied a more dominant zinc-rich phase at the surface before cycling for $LiZn_{500}$ and $Li_{rp}Zn_{500}$. The slightly higher surface potential for $Li_{rp}Zn_{500}$ indicates a stronger lithiated intermetallic phase since pure lithium should be in the range of +1.4 V (Figure 2b; Figure S6, Supporting Information). This was enabled by stronger interaction between lithium and zinc from the native layer dilution. Figure 5 provides the surface morphological variations of Li_{rp} and $Li_{rp}Zn_{500}$ before and after Li electrodeposition/-dissolution. Li_{rp} has a denser HSAL growth and less pit formation at the

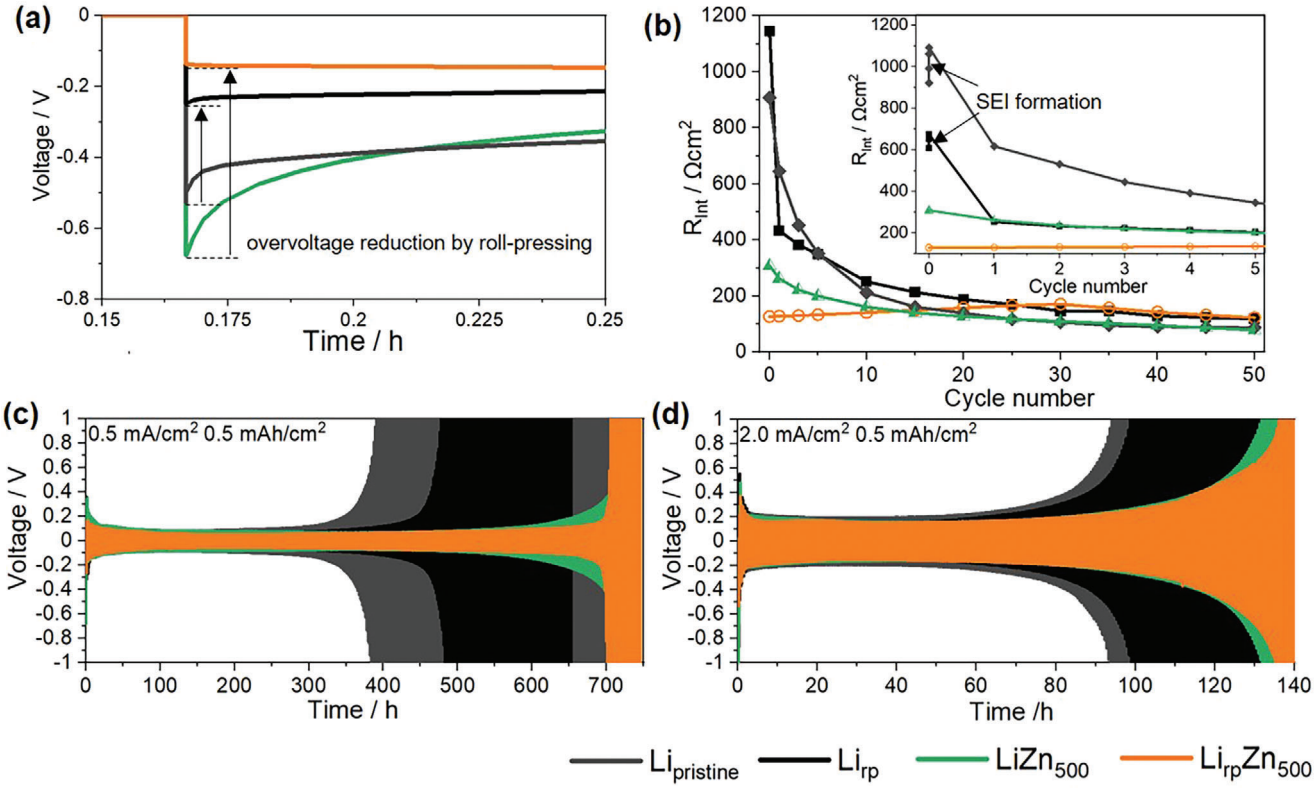

Figure 6. Comparison of a) overvoltage profiles from the first electrodeposition, b) evolution of R_{int} from EIS measured in a frequency range between 0.1 MHz and 0.1 Hz during the first 50 cycles with a magnification of the first 10 cycles and galvanostatic cycling at c) 0.5 mA cm^{-2} and d) 2.0 mA cm^{-2} with a capacity of 0.5 mAh cm^{-2} of symmetric cells with $Li_{pristine}$, Li_{rp}, $LiZn_{500}$, and $Li_{rp}Zn_{500}$.

surface compared to $Li_{pristine}$ ($Li_{pristine}$: Figure 4a and Li_{rp}: Figure 5b). Moreover, the cross-section revealed an overall thinner HSAL layer on the surface of the Li_{rp} and pits that were completely filled with HSAL. The HSAL were more attached to the surface than with $Li_{pristine}$, which was attributed to the better electrical contact from native layer dilution by roll-pressing. $Li_{rp}Zn_{500}$ initially exhibited no noteworthy difference from $LiZn_{500}$ in top-view images ($LiZn_{500}$: Figure 4g and $Li_{rp}Zn_{500}$: Figure 5e), whereas cross-section images revealed an intermetallic coating with less curvature and smoother surface (Figure 4f). The irregularities of the intermetallic coating from $LiZn_{500}$ presumably lead to premature cracking of the intermetallic coating at areas with highest curvature, severe HSAL growth at cracked regions resulting in an accelerated dissolution of the intermetallic coating into the HSAL and Li bulk. Therefore, a smoother and more uniform coating revealed a higher stability upon prolonged electrodeposition/-dissolution accompanied by a delayed cracking of the intermetallic coating (**Figure 6**).

The roll-press method reduced the nucleation overvoltage in the first cycle for uncoated Li foil by 53% ($Li_{pristine}$: −0.53 V; Li_{rp}: −0.25 V; Table S1, Supporting Information) and for the coated Li foil by 81% ($LiZn_{500}$: −0.67 V; $Li_{rp}Zn_{500}$: −0.13 V; Figure 6a, Table S1, Supporting Information). The overvoltage reduction showed a lower kinetical hindrance for Li electrodeposition due to a facilitated Li ion transport through the electrode/electrolyte interphase.[57] Similar effects were apparent in the evolution of the interphase resistance upon prolonged galvanostatic cycling (Figure 6b). In addition, the SEI formation at the Li surface before cycling was visible by an increase of the initial R_{int} under open circuit conditions for $Li_{pristine}$ and Li_{rp} (magnified graph for the first ten cycles). $LiZn_{500}$ and $Li_{rp}Zn_{500}$ showed a constant initial R_{int} due to the protective properties of the intermetallic coating against electrolyte decomposition. During the electrodeposition/-dissolution process, R_{int} decreased within the first 30 cycles for $Li_{pristine}$ from 1606 to 189 Ω and for Li_{rp} from 1144 to 147 Ω. $LiZn_{500}$ showed a R_{int} of 546 Ω and approached $Li_{pristine}$ and Li_{rp} after 30 cycles with 195 Ω. The decrease of R_{int} with the rising cycle number was interpreted as an increase in surface area due to pit formation and HSAL growth.[57] In contrast, $Li_{rp}Zn_{500}$ has the lowest initial R_{int} and showed only a minor increase from 127 to 171 Ω within the first 30 cycles emphasizing a facilitated Li ion diffusion through the intermetallic coating compared to the R_{int} progression of $LiZn_{500}$. The minor R_{int} increase of $Li_{rp}Zn_{500}$ was presumably caused by the formation of a thin SEI film on top of the intermetallic coating. The nearly constant R_{int} during prolonged electrodeposition/-dissolution indicated an intermetallic protective coating with higher stability and low resistance. Beyond the first cycle analysis and progression of R_{int}, the pre-treated and/or coated samples were analyzed in a symmetric cell setup at different current densities (Figure 6c,d; Figure S7b, Supporting Information). At low current densities (Figure 6c, for 0.5 mA cm^{-2}) the Li_{rp} showed a 24% increase in cycle number compared to $Li_{pristine}$ before reaching the cut-off voltage ($Li_{pristine}$: 390 cycles, Li_{rp}: 482 cycles). The cut-off voltage for

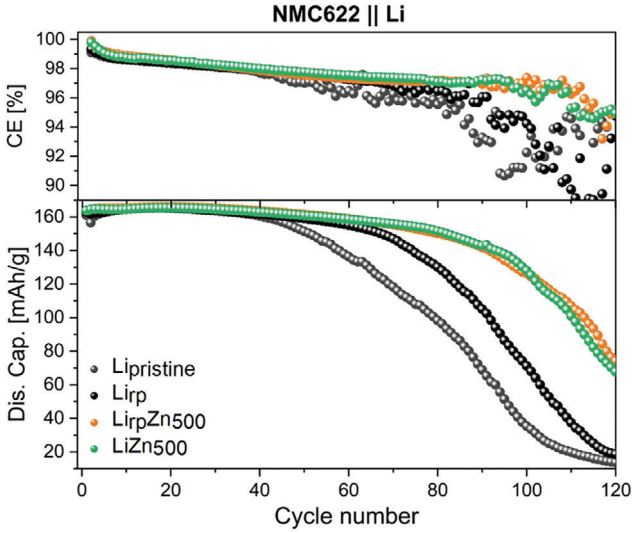

Figure 7. Coulombic efficiency (CE) and specific discharge capacity of the NMC622||Li cells assembled with different Li metal anodes: $Li_{pristine}$, Li_{rp}, $LiZn_{500}$, and $Li_{rp}Zn_{500}$ and cycled at 0.2 C in a voltage range of 3.0–4.3 V.

the $Li_{rp}Zn_{500}$||$Li_{rp}Zn_{500}$ cell was reached at 700 cycles thus earlier than the $LiZn_{500}$||$LiZn_{500}$ cell. However, this trend was only observed for the low current density and prolonged cycle life for $Li_{rp}Zn_{500}$||$Li_{rp}Zn_{500}$ was demonstrated for 1.0 and 2.0 mA cm^{-2} (Figure 6d; Figure S7b, Supporting Information). The combination of roll-pressing as a pre-treatment with an optimized intermetallic coating thickness revealed a prolonged cycle life, lower overvoltage due to a higher Li ion diffusion, homogeneously distributed Li electrodeposition/-dissolution, and protection of the subjacent Li reservoir.

Finally, $Li_{pristine}$, Li_{rp}, $LiZn_{500}$, and $Li_{rp}Zn_{500}$ were analyzed in an $LiNi_{0.6}Mn_{0.2}Co_{0.2}O_2$||Li based (NMC622||Li, NMC622||LiZn) cell setup (**Figure 7**). The initial specific capacity of the investigated cells based on different anode materials was similar at the beginning since the specific capacity is determined by the NMC622-based cathode. After a constant phase within the initial 40 cycles, the specific discharge capacity of $Li_{pristine}$ dropped first, followed by Li_{rp}. A decrease in specific discharge capacity to 50% was reached after 87 cycles for $Li_{pristine}$ and 97 cycles for Li_{rp}. The cycle life was further increased for $LiZn_{500}$ with 115 cycles and for $Li_{rp}Zn_{500}$ with 118 cycles until 50% capacity retention. The positive impact of roll-pressing Li metal foils on capacity retention was demonstrated by NMC622||Li_{rp} and NMC622||$Li_{rp}Zn_{500}$ cells, while the beneficial effect of the LiZn-intermetallic coating was confirmed by the NMC622||$LiZn_{500}$ and NMC622||$Li_{rp}Zn_{500}$ cells. In this study, the experimental setup involved a standard electrolyte, a coin cell setup with non-optimized internal pressure, and a thin Li metal foil. Therefore, an optimized cell setup is expected to notably improve the cycle life by implementing roll-pressed Li metal with an intermetallic coating.

A summary of the influence given by roll-pressing of Li metal and in combination with the coating by thermal evaporation during electrodeposition/-dissolution was schematically illustrated in (**Figure 8**). Therein, roll-pressing of lithium leads to a decrease in surface roughness and dilution of the native layer thickness, whereas pristine Li foil is displayed with a distinctive surface pattern. In the second step, Zn is coated via thermal evaporation to form the LiZn-intermetallic phase on the Li foil, adopting the subjacent surface pattern. Subsequently, the difference between the intermetallic coating on $Li_{pristine}$ and Li_{rp} after progressing electrodeposition/-dissolution is illustrated. Therein, $Li_{pristine}$ shows a rough surface with higher curvature after coating. Regions with a higher curvature experience major surface cracks and dissolution of the intermetallic coating. A more pronounced HSAL growth is evident after electrodeposition/-dissolution leading to a reduced cycle life. The intermetallic coating on Li_{rp} has a smooth surface and shows less pronounced HSAL growth after electrodeposition and -dissolution, enabling this type of electrode to reach a longer cycle life.

3. Conclusion

In this study, thermal evaporation of Zn was used as a coating method to form a protective intermetallic coating on Li metal to reduce detrimental surface reactions and increase the cycling stability in LMBs. Zn metal was selected due to its low cost and high diffusion coefficient of the formed LiZn-intermetallic phase.

In the first step, the coating thickness on pristine Li metal foil was optimized and the formation of the LiZn-intermetallic phase was confirmed by XRD. The thickness of the formed intermetallic coating was determined with a cross-sectional analysis prepared under cryogenic conditions. LSM analysis of the coated surface revealed a more pronounced roughness with increasing intermetallic coating thickness due to the high roughness of the subjacent $Li_{pristine}$ and the volumetric expansion during the formation of the intermetallic phase. An enhanced pit and HSAL growth together with a cracking of the intermetallic coating after 20 cycles was observed for uncoated $Li_{pristine}$, $LiZn_{100}$, and $LiZn_{250}$. In contrast, $LiZn_{500}$ was found to have an intact intermetallic coating and HSAL growth below and above the coating. The higher stability of $LiZn_{500}$ was also reflected by electrochemical analysis, with a 90% increase in cycle number from $Li_{pristine}$ to $LiZn_{500}$ before reaching the cut-off voltage at low current densities.

In the second step, the subjacent, pristine Li foil was optimized by roll-pressing. LSM and KPFM measurements confirmed a reduced surface roughness and dilution of the native layer after roll-pressing pristine Li metal. This was followed by coating Li_{rp} and an evaluation of the combinational influence from the pre-treatment and coating. The LiZn-intermetallic coating based on 500 nm Zn-coating on roll-pressed Li foil also induced a smoother intermetallic surface with a stronger lithiated phase, as suggested from surface potential measurements by KPFM. The advantages of combining pre-treatment and coating were also evident in the electrochemical analysis, with $Li_{rp}Zn_{500}$ exhibiting the lowest overpotential, R_{int}, and longest cycle life in symmetric cells. Cross-section images after 20 cycles revealed a smoother surface with less curvature for $Li_{rp}Zn_{500}$ compared to $LiZn_{500}$. The intermetallic coating showed at areas with higher curvature an accelerated cracking of the coating and enhanced HSAL growth after electrodeposition/-dissolution. To confirm the beneficial effect of the combinational approach and its potential to enable the commercialization of LMBs, NMC622||Li cells with modified Li electrodes were analyzed and revealed a prolonged cycle life and superior performance. Overall, the intermetallic

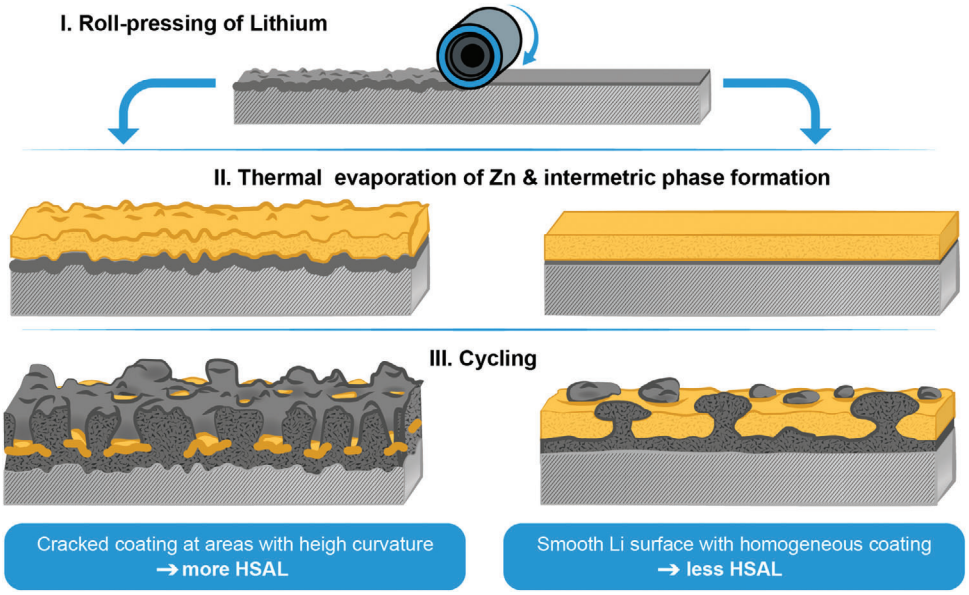

Figure 8. Schematic illustration of the influence of roll-pressing Li foil and subsequent Zn-coating by thermal evaporation (PVD). I. reduction of the surface roughness and native layer dilution by roll-pressing Li metal. II. Deposition of a Zn-coating and intermetallic phase formation on pristine and roll-pressed Li foil with indicated curvature by arrows for the coated $Li_{pristine}$ foil. III. Major surface cracks and more pronounced HSAL growth for coated $Li_{pristine}$ and less surface cracks and HSAL growth for coated Li_{rp} with progressing electrodeposition/-dissolution.

coating led to an extended cycle life by improving the electrodeposition and -dissolution behavior of Li ions on the surface and mitigating the degradation processes between Li and electrolyte during cycling, which resulted in a reduced Li consumption. However, the cross-sectional images showed that the intermetallic layer dissolved during cycling experiments, especially in areas with higher curvature, leading to preferential electrodeposition/-dissolution of Li in these areas and accelerated consumption of Li bulk. It is therefore important to further develop and improve intermetallic coatings in order to reduce the dissolution and cracking during cycling.

4. Experimental Section

Materials: Battery-grade Li metal was purchased from Honjo Lithium with thicknesses of 130 and 500 µm. Li metal with a thickness of 500 µm was roll-pressed to a final thickness of 130 µm between two siliconized polyester foils (50 µm, PPI Adhesive Products GmbH) using a roll-press calender (GK300L, Saueressig) within a dry room (dew point <−60 °C). Li metal foils were then transferred under an atmospheric exclusion in an Ar-filled glovebox (H_2O and O_2 values <0.1 ppm) for coating or electrode preparation.

Physical Vapor Deposition by Thermal Evaporation: The coating process was performed in a ProVap PVD System (MBraun) placed in an Ar-filled glovebox (H_2O and O_2 values <0.1 ppm). This system was based on a resistive heating approach, where a high electric current and low voltage were applied to melt and vaporize the source material. Li metal foil (130 µm) was placed on the substrate holder inside the PVD chamber facing down to the evaporation source to coat different thicknesses at a rate of 0.5 nm s^{-1}. In this study, 100, 250, and 500 nm Zn were deposited in Li foil. For the coating process, Zinc (Zn) pellets (Sigma–Aldrich, 99.99 %) were placed in a Wolfram evaporation boat, connected to a power supply. The deposition rate was controlled by an SQC-310 controller (Inficon) operating at 6 MHz during the evaporation process. The substrate was protected by a shutter until the desired deposition rate was reached and a shutter above the coating material protected the substrate against outgassing products.

Electrochemical Investigations: Li metal electrodes and Zn-coated Li metal electrodes were characterized in a CR2032-type two-electrode[60] coin cell for symmetric cells (Li||Li or LiZn||LiZn) and $LiNi_{0.6}Mn_{0.2}Co_{0.2}O_2$||Li based cells (NMC622||Li, NMC622||LiZn) and cycled at 20 °C using a MACCOR battery cycler (MACCOR series 4000). Symmetric coin cells were assembled in an Ar-filled glovebox (H_2O and O_2 values <0.1 ppm) using ∅12 mm Li electrodes and a ∅13 mm separator (2x Freudenberg (FS2190), 2xCelgard 2500) with 60 µL electrolyte containing 1 M $LiPF_6$ in EC/EMC (3:7 by weight, EC: ethylene carbonate, EMC: ethyl methyl carbonate) combined with two spacers (thickness 2 × 0.5 mm). NMC622||Li cells were assembled under equivalent conditions, but a different cell setup including a ∅13 mm Li electrode, ∅12 mm NMC622-based positive electrode, and ∅14 mm separator (2x Freudenberg (FS2190), 2xCelgard 2500) with 80 µL electrolyte and two spacers (thickness 1 × 0.5 mm, 1 × 1.0 mm). For symmetric cells, the current density was varied from 0.5 to 2 mA cm^{-2} with a constant capacity of 0.5 mAh cm^{-2} for long-term cycling experiments and cut-off criteria of −1.5 to +1.5 V. The NMC622||Li cells were cycled after a rest period of 5 h in a voltage range of 3.0–4.3 V at a charge/discharge rate of 0.2C (1C corresponds to 180 mA g^{-1}). As positive electrode 95% NMC622 (BASF) as active material, 2% conductive additive (Super C65, IMERYS) and 3% polyvinylidene fluoride (PVDF) binder (Solvay) was used to obtain positive electrodes with an areal capacity of 2.3 mAh cm^{-2} produced in an in-house battery line. The electrode sheets were pre-dried under vacuum ($3 \cdot 10^{-3}$ mbar) at 100 °C for 12 h and then punched into ∅12 mm electrodes.

Electrochemical impedance spectroscopy (EIS) was measured using a VMP3 potentiostat (Bio-152 Logic) in a frequency range between 0.1 MHz and 0.1 Hz with an amplitude of 10 mV. For the EIS analysis combined with galvanostatic cycling symmetric Li||Li coin cells were used and after cell assembly EIS was measured four times under open circuit conditions. Li||Li cells were cycled at 1.0 mA cm^{-2} and 0.5 mAh cm^{-2} and EIS was measured after each cycle for the first 10 cycles and then after every fifth cycle up to 50 cycles.

Characterization Methods: The surface morphology of pristine, coated, and cyclic-aged Li electrodes was investigated by scanning electron

microscopy (SEM) using a CrossBeam 550 working station from Carl–Zeiss with a field emission gun at an acceleration voltage of 3 kV and a working distance of 5.1 mm. For SEM characterization, symmetric cells were dissembled after 20 cycles at 0.5 mA cm^{-2} and 0.5 mAh cm^{-2}. The cross-sections were prepared under cryogenic conditions with an accelerating voltage of 30 kV and a current ranging from 7–30 nA at a temperature of −160 °C to maintain the morphology of the samples by preventing Li melting effects. The samples were integrated inside an Ar-filled glovebox in a custom-made cryo-transfer module (Kammrath & Weiss), transferred into the SEM chamber, and connected to liquid N_2 and a temperature control element. The temperature was set to −160 °C and was maintained for 10 min before the cross-section preparation was started by fast ion beam (FIB). Cross-sections of aged electrodes were conducted in areas with HSAL growth next to intact surfaces.

The elemental composition of the electrode surface and cross-section was investigated by energy-dispersive X-ray spectroscopy (EDX) with an Ultim Extreme detector from Oxford Instruments and evaluated with the AZtech software from Oxford Instruments at an SEM accelerating voltage of 5 kV and a current of 1 nA.

The phase structure analysis of the Zn-coated Li metal was performed by X-ray diffraction (XRD) on a D8 Advance diffractometer (Bruker) with a Cu-Kα irradiation ($\lambda = 0.15418$ nm) and with a divergence slit of 0.5°. The coated Li metal was placed on a sample holder (single-crystal silicon) and fixed with polyimide film (capton foil) to protect the Li metal from air.

Kelvin Probe Force Microscopy (KPFM): KPFM measurements were performed with a Cypher ES atomic force microscope (AFM, Oxford Instruments) using ASYELEC-01-R2 tips with a Ti/Ir coating. Measurements were performed in a dual-pass experiment with a delta height of 30 nm during KPFM data acquisition. The samples were prepared in an Ar-filled glovebox and measured in Ar at a constant sample temperature of 32 °C (instrument standard temperature).

Supporting Information

Supporting Information is available from the Wiley Online Library or from the author.

Acknowledgements

The authors would like to acknowledge the financial support from the German Federal Ministry of Education and Research (BMBF) within the project ProLiFest (03XP0253A) and to the European Union's Horizon Europe Research and Innovation Program within the project PSIONIC under Grant Agreement No. 101069703. In addition, the authors would like to thank Andre bar for the graphics support.

Open access funding enabled and organized by Projekt DEAL.

Conflict of Interest

The authors declare no conflict of interest.

Data Availability Statement

The data that support the findings of this study are available on request from the corresponding author. The data are not publicly available due to privacy or ethical restrictions.

Keywords

cryo-FIB/SEM, intermetallic protective coating, lithium metal anode, roll-pressing, thermal evaporation

Received: October 4, 2023
Revised: December 15, 2023
Published online: March 14, 2024

[1] T. Placke, R. Kloepsch, S. Dühnen, M. Winter, *J. Solid State Electrochem.* **2017**, *21*, 1939.
[2] R. Wagner, N. Preschitschek, S. Passerini, J. Leker, M. Winter, *J. Appl. Electrochem.* **2013**, *43*, 481.
[3] O. Gröger, H. A. Gasteiger, J.-P. Suchsland, *J. Electrochem. Soc.* **2015**, *162*, 2605.
[4] D. Bresser, K. Hosoi, D. Howell, H. Li, H. Zeisel, K. Amine, S. Passerini, *J. Power Sources* **2018**, *382*, 176.
[5] R. Schmuch, R. Wagner, G. Hörpel, T. Placke, M. Winter, *Nat. Energy* **2018**, *3*, 267.
[6] J. B. Goodenough, K.-S. Park, *J. Am. Chem. Soc.* **2013**, *135*, 1167.
[7] M. S. Whittingham, *Chem. Rev.* **2014**, *114*, 11414.
[8] J. Liu, Z. Bao, Y. Cui, E. J. Dufek, J. B. Goodenough, P. Khalifah, Q. Li, B. Y. Liaw, P. Liu, A. Manthiram, Y. S. Meng, V. R. Subramanian, M. F. Toney, V. V. Viswanathan, M. S. Whittingham, J. Xiao, W. Xu, J. Yang, X.-Q. Yang, J.-G. Zhang, *Nat. Energy* **2019**, *4*, 180.
[9] E. Peled, *J. Electrochem. Soc.* **1979**, *126*, 2047.
[10] D. Aurbach, Y. Ein-Ely, A. Zaban, *J. Electrochem. Soc.* **1994**, *141*, L1.
[11] M. Winter, *Z. Phys. Chem.* **2009**, *223*, 1395.
[12] J. O. Besenhard, M. Winter, *Pure Appl. Chem.* **1998**, *70*, 603.
[13] J. Heine, P. Hilbig, X. Qi, P. Niehoff, M. Winter, P. Bieker, *J. Electrochem. Soc.* **2015**, *162*, 1094.
[14] M.-H. Ryou, Y. M. Lee, Y. Lee, M. Winter, P. Bieker, *Adv. Funct. Mater.* **2015**, *25*, 834.
[15] E. Peled, S. Menkin, *J. Electrochem. Soc.* **2017**, *164*, 1703.
[16] W. Xu, J. Wang, F. Ding, X. Chen, E. Nasybulin, Y. Zhang, J.-G. Zhang, *Energy Environ. Sci.* **2014**, *7*, 513.
[17] K.-H. Chen, K. N. Wood, E. Kazyak, W. S. LePage, A. L. Davis, A. J. Sanchez, N. P. Dasgupta, *J. Mater. Chem. A* **2017**, *5*, 11671.
[18] L. Hellweg, T. Beuse, M. Winter, M. Börner, *J. Electrochem. Soc.* **2023**, *170*, 040530.
[19] S. Stuckenberg, M. M. Bela, C. T. Lechtenfeld, M. Mense, V. Küpers, T. T. K. Ingber, M. Winter, M. C. Stan, *Small* **2023**, *20*, 2305396.
[20] S. Park, H. J. Jin, Y. S. Yun, *Adv. Mater.* **2020**, *32*, 2002193.
[21] T. T. K. Ingber, M. M. Bela, F. Püttmann, J. F. Dohmann, P. Bieker, M. Börner, M. Winter, M. C. Stan, *J. Mater. Chem. A* **2023**, *11*, 17828.
[22] J. Cao, Y. Xie, Y. Yang, X. Wang, W. Li, Q. Zhang, S. Ma, S. Cheng, B. Lu, *Adv. Sci.* **2022**, *9*, 2104689.
[23] D. Liebenau, K. Jalkanen, S. Schmohl, M. C. Stan, P. Bieker, H. D. Wiemhöfer, M. Winter, M. Kolek, *Adv. Mater. Interfaces* **2019**, *6*, 1900518.
[24] R. Xu, X.-B. Cheng, C. Yan, X.-Q. Zhang, Y. Xiao, C.-Z. Zhao, J.-Q. Huang, Q. Zhang, *Matter* **2019**, *1*, 317.
[25] D. Kang, M. Xiao, J. P. Lemmon, *Batteries Supercaps* **2020**, *4*, 445.
[26] H. Wang, Y. Liu, Y. Li, Y. Cui, *Electrochem. Energy Rev.* **2019**, *2*, 509.
[27] Y. Xie, W. Zheng, J. Ao, Y. Shao, X. Huang, H. Li, S. Cheng, X. Wang, *Energy Storage Mater.* **2023**, *62*, 102925.
[28] N. Delaporte, Y. Wang, K. Zaghib, *Front. Mater.* **2019**, *6*, 1.
[29] Z. Han, C. Zhang, Q. Lin, Y. Zhang, Y. Deng, J. Han, D. Wu, F. Kang, Q. H. Yang, W. Lv, *Small Meth.* **2021**, *5*, 2001035.
[30] Z. Yu, Y. Cui, Z. Bao, *Cell Rep. Phys. Sci.* **2020**, *1*, 100119.
[31] M. Peng, K. Shin, L. Jiang, Y. Jin, K. Zeng, X. Zhou, Y. Tang, *Angw. Chem.* **2022**, *61*, 202206770.
[32] B. Sun, J. Lang, K. Liu, N. Hussain, M. Fang, H. Wu, *Chem. Comm.* **2019**, *55*, 1592.
[33] X. Liang, Q. Pang, I. R. Kochetkov, M. S. Sempere, H. Huang, X. Sun, L. F. Nazar, *Nat. Energy* **2017**, *2*, 17119.
[34] A. Kolesnikov, D. Zhou, M. Kolek, J. P. B. Jimenez, P. Bieker, M. Winter, M. C. Stan, *J. Electrochem. Soc.* **2019**, *166*, A1400.
[35] M. C. Stan, J. Becking, A. Kolesnikov, B. Wankmiller, J. E. Frerichs, M. R. Hansen, P. Bieker, M. Kolek, M. Winter, *Mater. Today* **2020**, *39*, 137.
[36] E. Kazyak, K. N. Wood, N. P. Dasgupta, *Chem. Mater.* **2015**, *27*, 6457.

[37] A. C. Kozen, C.-F. Lin, A. J. Pearse, M. A. Schroeder, X. Han, L. Hu, S.-B. Lee, G. W. Rubloff, M. Noked, *ACS Nano* **2015**, *9*, 5884.
[38] S. Lobe, A. Bauer, S. Uhlenbruck, D. Fattakhova-Rohlfing, *Adv. Sci.* **2021**, *8*, 2002044.
[39] N. Delaporte, A. Perea, S. Collin-Martin, M. Léonard, J. Matton, V. Gariepy, H. Demers, D. Clément, E. Rivard, A. Vijh, *Batteries Supercaps* **2022**, *5*, 202200245.
[40] J. Deng, Y. Wang, S. Qu, Y. Liu, W. Zou, F. Zhou, A. Zhou, J. Li, *Batteries Supercaps* **2020**, *4*, 140.
[41] Z. Zhang, Y. Jin, Y. Zhao, J. Xu, B. Sun, K. Liu, H. Lu, N. Lv, Z. Dang, H. Wu, *Nano Res.* **2021**, *14*, 3999.
[42] M. Nicolaus, M. Schäpers, *Modern Surface Technology*, Wiley-VCH Verlag GmbH & Co. KGaA, Weinheim, **2006**.
[43] D. M. Mattox, *Handbook of Physical Vapor Deposition (PVD) Processing*, Elsevier Science, Norwich NY Oxford, **2010**.
[44] J. Wang, P. King, R. A. Huggins, *Solid State Ionics* **1985**, *20*, 185.
[45] A. Anani, S. Crouch-Baker, R. A. Huggins, *Electrochem. Soc.* **1986**, *18*, 457.
[46] R. A. Huggins, *J. Power Sources* **1999**, *13*, 81.
[47] S. Jin, Y. Ye, Y. Niu, Y. Xu, H. Jin, J. Wang, Z. Sun, A. Cao, X. Wu, Y. Luo, H. Ji, L.-J. Wan, *J. Am. Chem. Soc.* **2020**, *142*, 8818.
[48] A. D. Pelton, *J. Phase Equilib. Diffus.* **1991**, *12*, 42.
[49] J. Becking, A. Gröbmeyer, M. Kolek, U. Rodehorst, S. Schulze, M. Winter, P. Bieker, M. C. Stan, *Adv. Mater. Interfaces* **2017**, *4*, 1700166.
[50] X. Qiu, X. Liu, S. Jiang, G. Jiang, Q. Zhang, *J. Iron Steel Res. Int.* **2021**, *28*, 1047.
[51] B. Wolff, F. Hausen, *J. Electrochem. Soc.* **2023**, *170*, 010534.
[52] S.-K. Otto, T. Fuchs, Y. Moryson, C. Lerch, B. Mogwitz, J. Sann, J. Janek, A. Henss, *ACS Appl. Energy Mater.* **2021**, *4*, 12798.
[53] C. Zhu, T. Fuchs, S. A. L. Weber, F. H. Richter, G. Glasser, F. Weber, H.-J. Butt, J. Janek, R. Berger, *Nat. Comm.* **2023**, *14*, 1300.
[54] R. Zhang, X.-R. Chen, X. Chen, X.-B. Cheng, X.-Q. Zhang, C. Yan, Q. Zhang, *Angew. Chem., Int. Ed.* **2017**, *56*, 7764.
[55] K. Yan, Z. Lu, H.-W. Lee, F. Xiong, P.-C. Hsu, Y. Li, J. Zhao, S. Chu, Y. Cui, *Nat. Energy* **2016**, *1*, 16010.
[56] L. Gireaud, S. Grugeon, S. Laruelle, B. Yrieix, J. M. Tarascon, *Electrochem. Commun.* **2006**, *8*, 1639.
[57] G. Bieker, M. Winter, P. Bieker, *Phys. Chem. Chem. Phys.* **2015**, *17*, 8670.
[58] A. J. Sanchez, E. Kazyak, Y. Chen, K.-H. Chen, E. R. Pattison, N. P. Dasgupta, *ACS Energy Lett.* **2020**, *5*, 994.
[59] S.-K. Otto, Y. Moryson, T. Krauskopf, K. Peppler, J. Sann, J. Janek, A. Henss, *Chem. Mater.* **2021**, *33*, 859.
[60] R. Nölle, K. Beltrop, F. Holtstiege, J. Kasnatscheew, T. Placke, M. Winter, *Mater. Today* **2020**, *32*, 131.